

## Shape and Rotational Motion Models for Tumbling and Monolithic Asteroid 2012 TC<sub>4</sub>:High Time Resolution Lightcurve with the Tomo-e Gozen Camera

SEITARO URAKAWA,<sup>1</sup> RYOU OHSAWA,<sup>2</sup> SHIGEYUKI SAKO,<sup>2</sup> SHIN-ICHIRO OKUMURA,<sup>1</sup> YURI SAKURAI,<sup>3</sup> JUN TAKAHASHI,<sup>4</sup> KAZUYOSHI IMAMURA,<sup>5</sup> HIROYUKI NAITO,<sup>6</sup> FUMITAKE WATANABE,<sup>6</sup> RYOMA NAGAYOSHI,<sup>6</sup> YASUHIKO MURAKAMI,<sup>6</sup> RYO OKAZAKI,<sup>7</sup> TOMOHIKO SEKIGUCHI,<sup>7</sup> MASATERU ISHIGURO,<sup>8</sup> TATSUHIRO MICHIKAMI,<sup>9</sup> AND MAKOTO YOSHIKAWA<sup>10</sup>

<sup>1</sup>Japan Spaceguard Association, Bisei Spaceguard Center 1716-3 Okura, Bisei, Ibara, Okayama 714-1411, Japan

<sup>2</sup>Institute of Astronomy, Graduate School of Science, The University of Tokyo, 2-21-1 Osawa, Mitaka, Tokyo 181-0015, Japan

<sup>3</sup>Department of Earth Science, Okayama University, 1-1-1 Kita-ku Tsushimanaka, Okayama 700-8530, Japan

<sup>4</sup>Center for Astronomy, University of Hyogo 407-2 Nishigaichi, Sayo, Hyogo 679-5313, Japan

<sup>5</sup>Anan Science Center, 8-1 Nagakawa Kamifukui Minami-Kawabuchi, Anan, Tokushima 779-1243, Japan

<sup>6</sup>Nayoro Observatory, 157-1 Nisshin, Nayoro, Hokkaido 096-0066, Japan

<sup>7</sup>Asahikawa Campus, Hokkaido University of Education, 9 Hokumon, Asahikawa, Hokkaido 070-8621, Japan

<sup>8</sup>Department of Physics and Astronomy, Seoul National University, 1 Gwanak-ro, Gwanak-gu, Seoul 08826, Korea

<sup>9</sup>Faculty of Engineering, Kindai University, Hiroshima Campus, 1 Takaya Umenobe, Higashi-Hiroshima, Hiroshima 739-2116, Japan

<sup>10</sup>Institute of Space and Astronautical Science, Japan Aerospace Exploration Agency, 3-1-1 Yoshinodai, Chuo-ku, Sagami-hara, Kanagawa, 252-5210, Japan

(Received November 15, 2018; Revised February 7, 2019; Accepted February 21, 2019)

Submitted to AJ

### ABSTRACT

We present visible and near-infrared observations of a near-Earth object (NEO), 2012 TC<sub>4</sub>. The NEO 2012 TC<sub>4</sub> approached close to the Earth at a distance of about 50,000 km in October 2017. This close approach provided a practical exercise for planetary defense. This apparition was also an appropriate opportunity to investigate 2012 TC<sub>4</sub>, which is a monolithic asteroid (Polishook 2013). We conducted the observation campaign of 2012 TC<sub>4</sub> using six small- and medium-sized telescopes. The multiband photometry analysis showed that the taxonomic class of 2012 TC<sub>4</sub> to be an X-type. In particular, we successfully obtained the high time resolution lightcurve of 2012 TC<sub>4</sub> with the Tomo-e Gozen camera, which is the world’s first wide-field CMOS camera, mounted on the 1.05 m Schmidt telescope at Kiso Observatory. The shape and rotational motion models of 2012 TC<sub>4</sub> were derived from the lightcurve. When 2012 TC<sub>4</sub> was assumed to be a triaxial ellipsoid, the rotational and precession periods were  $8.47 \pm 0.01$  min and  $12.25 \pm 0.01$  min, respectively, with the long axis mode. This indicates that 2012 TC<sub>4</sub> is a tumbling and monolithic asteroid. The shape models showed that the plausible axial lengths to be  $6.2 \times 8.0 \times 14.9$  m or  $3.3 \times 8.0 \times 14.3$  m. The flattened and elongated shape indicates that 2012 TC<sub>4</sub> is a fragment produced by a impact event. We also estimated the excitation timescale, which implied that the impact event happened within  $\sim 3 \times 10^5$  yr and 2012 TC<sub>4</sub> has a fresh surface.

*Keywords:* minor planets, asteroids: individual (2012 TC<sub>4</sub>), instrumentation: detectors

### 1. INTRODUCTION

“Planetary Defense” or “Spaceguard” refers to a number of efforts against asteroid impact hazard. A spaceguard effort discovers near-Earth objects (NEOs), seeks their trajectory, and judges whether they will collide with the Earth. Representative NEO survey projects are Pan-STARRS (the Panoramic Survey Telescope and Rapid Response System, Wainscoat et al. 2014; Chambers & Pan-STARRS Team 2016), Catalina Sky Survey (Larson et al.

1998; Christensen et al. 2014), and NEOWISE (Mainzer et al. 2011a). There are many other ground-based survey projects and future space plans including ATLAS (Tonry 2011) and NEOCam (Mainzer et al. 2017). In addition to survey observations, it is also important to reveal the physical properties of each NEO by obtaining information regarding the rotational period, rotational motion, shape, and taxonomic class. In the event of an impact hazard, such information can assist in the development countermeasure, such as a kinetic impactor (Cheng et al. 2018). Moreover, fostering better understanding of NEOs helps to elucidate the planetary formation processes. Because NEOs have reflected the history of collision, destruction, and coalescence of small solar system bodies from the planet formation era. NEOs are also practically accessible object by spacecrafts. The physical properties that were estimated by the ground-based observations of asteroid (25143) Itokawa and asteroid (162173) Ryugu became essential information for the Hayabusa and Hayabusa-2 projects (Kaasalainen et al. 2003; Ostro et al. 2005; Kim et al. 2013; Ishiguro et al. 2014; Müller et al. 2017). Furthermore, the technological progress brought on by explorations provides new prospects, such as manned explorations and resource collections of NEOs (Abell et al. 2016). Exploration technology will also return to the spaceguard efforts as an impact avoidance technology.

Hayabusa, Hayabusa-2, NEAR, and OSIRIS-Rex are representative NEO spacecrafts. The exploration of Itokawa by Hayabusa revealed that Itokawa was covered with numerous boulders and possessed rubble-pile structures due to weak gravity constraints (Fujiwara et al. 2006). An asteroid that consists of a single boulder is sometimes called a monolithic asteroid. The physical properties of a monolithic asteroid, which could be the smallest unit constituting a rubble-pile asteroid, can provide clues to clarify the formation process of boulders in destructive collisions. An asteroid's rotational period is an important indicator to distinguish monolithic and rubble-pile asteroids. Although cohesive force might prevent the rotational breakup (Rozitis et al. 2014), most asteroids rotating shorter than the period of 2.2 hr are considered to be monolithic asteroids because the fast rotation makes it difficult to keep the rubble-pile structure due to the strong centrifugal force (Pravec & Harris 2000). Almost all monolithic asteroids are NEOs smaller than 200 m in diameter. Such NEOs are confirmed to be monolithic asteroids by measuring their rotational periods, immediately after being discovered by survey observations. Physical properties of monolithic asteroids, such as the taxonomic class and shape, are hardly determined, except for the rotational period and rough diameter. In order to estimate the taxonomic class, spectroscopic observations or multiband photometry is required. However, the small size and faintness of monolithic asteroids make it difficult to conduct spectroscopic observation, which demand sufficient brightness. In the case of the multiband photometry, since the brightness of monolithic asteroids inevitably changes due to the fast rotation during the switching of the filter, we need to calibrate the brightness change appropriately. The calibration requires to obtain the accurate lightcurve data that cover the whole rotational phase of the monolithic asteroids. Otherwise, we need to calibrate the monolithic asteroids with a multiband simultaneous camera without the switching of the filter. Spectroscopic observations and multiband photometry are not carried out immediately after the discovery of NEOs. Furthermore, the estimation of shape is required the enough amount of lightcurve data that are obtained by the observation of asteroid from various directions. To observationally deduce the taxonomic class and shape of the monolithic asteroids, the closest day-of-approach of the target asteroid to the Earth should be known in advance.

The purpose of our study is to obtain the shape and rotational motion model of a NEO, 2012 TC<sub>4</sub>, from a high time resolution lightcurve. Furthermore, we deduce the taxonomic class of 2012 TC<sub>4</sub> with the visible and near-infrared color indexes by multiband photometry. The NEO 2012 TC<sub>4</sub> was discovered by the Pan-STARRS on October 4, 2012, and approached the Earth with a distance of  $\sim 95,000$  km on October 12, 2012. The rotational period and diameter were estimated to be  $12.24 \pm 0.06$  min and 7-34 m, respectively (Polishook 2013). Therefore, 2012 TC<sub>4</sub> is supposed to be a monolithic asteroid. However, the shape and taxonomic class were not identified. In addition, the lightcurve of 2012 TC<sub>4</sub> was not fully explained by the period of 12.24 min. The NEO 2012 TC<sub>4</sub> approached the Earth again on October 2017. The closest approach distance was  $\sim 50,000$  km on October 12, 2017. This apparition was an appropriate observation opportunity to investigate the physical properties of a small monolithic asteroid. In particular, we could use the Tomo-e Gozen camera (Sako et al. 2016; Sako et al. 2018), which was a low-noise, high-quantum-efficiency, and super wide-field CMOS mosaic camera. The quick and contiguous readout capability of the Tomo-e Gozen camera assisted in the observation of 2012 TC<sub>4</sub>, which is both fast-rotating and fast-moving. In this paper, we deal with the following. In Section 2, we describe the observations and their data reduction, with particular focus on the Tomo-e Gozen camera. In Section 3, we mention the results of taxonomic class, diameter, shape and rotational motion. In Section 4, we discuss the impact event that could have been happened on the parent object of

2012 TC<sub>4</sub> and the excitation and damping timescales. Finally, we summarize the physical properties of 2012 TC<sub>4</sub> and mention the significance of elucidating the physical properties of 10 m-sized NEOs.

## 2. OBSERVATIONS AND DATA REDUCTION

### 2.1. Observations

We conducted the observation campaigns of 2012 TC<sub>4</sub> with six small- and medium-sized telescopes from October 9 to October 11, 2017. Since 2012 TC<sub>4</sub> moved to the dayside, we could not observe it on October 12, 2017, the day of the closest approach. The observational circumstances and states of 2012 TC<sub>4</sub> are listed in Tables 1 and 2, respectively. The longest observation of this campaign was carried out using the Tomo-e Gozen camera mounted on a 1.05 m  $f/3.1$  Schmidt telescope at Kiso Observatory. The Tomo-e Gozen is an extremely wide-field camera equipped with 84 CMOS sensors that consist of four modules with 21 CMOS sensors. The Tomo-e Gozen camera records an approximately 20 square degree area at a maximum frame rate of 2 Hz (= 0.5 s exposure). The field of view (FoV) for one CMOS sensor is 0.24 square degrees with a pixel resolution of 1.''2. The Tomo-e Gozen camera was not completed at the time 2012 TC<sub>4</sub> approached the Earth, but a performance test of the Tomo-e Gozen camera was conducted using a single module with four CMOS sensors. The time control accuracy of the Tomo-e Gozen camera was around 1 s in the performance test. The quick and contiguous readout capability of the Tomo-e Gozen camera is suitable for the observation of a fast-rotating and fast-moving asteroid, such as 2012 TC<sub>4</sub>. The lightcurve of 2012 TC<sub>4</sub> was obtained with high time resolution during the performance test. The exposure times were 10 s on October 9, 10 s and 5 s on October 10, and 2 s on October 11, 2017. To estimate the taxonomic class of 2012 TC<sub>4</sub>, spectroscopy was also conducted using the grism spectrometer of the Tomo-e Gozen camera with an exposure time of 5 s on October 11, 2017. However, the taxonomic class of 2012 TC<sub>4</sub> was not estimated, because it was not possible to carry out the adequate wavelength calibration during the performance test. Despite this, the zeroth-order light in the grism spectroscopy was used as the lightcurve data. No filter was used in the observation at Kiso Observatory.

The visible multiband photometry was performed using the 1.0 m  $f/3$  telescope at Bisei Spaceguard Center (BSGC) on October 10, 2017. The multiband photometry data was also used as the lightcurve. The detector of the 1.0 m telescope consisted of four CCD chips with  $4096 \times 2048$  pixels. We used one CCD chip to obtain as many images as possible by shortening the processing time. The FoV for one CCD chip is 0.65 square degrees with a pixel resolution of 1.''0. The multiband photometry data was obtained with Sloan Digital Sky Survey (SDSS)  $g'$ ,  $r'$ ,  $i'$ , and  $z'$  filters. The filters were changed in the following sequence: 5 - 7  $g'$  images  $\rightarrow$  5  $r'$  images  $\rightarrow$  5  $i'$  images  $\rightarrow$  6 - 8  $z'$  images  $\rightarrow$  5  $i'$  images  $\rightarrow$  5  $r'$  images  $\rightarrow$  5 - 7  $g'$  images. We repeated this sequence three times. All images were obtained with an exposure time of 120 s for each filter in the no-binning mode.

The near-infrared multiband photometry was carried out using the Nishiharima Infrared Camera (NIC) (Takahashi et al. 2014) mounted at the Cassegrain focus ( $f/12$ ) of the 2.0 m Nayuta telescope at Nishi-Harima Astronomical Observatory. The FoV of the NIC is  $2.''73 \times 2.''73$ . Since the NIC is a near-infrared three-band ( $J$ ,  $H$ , and  $K_s$ ) simultaneous camera, the color index of 2012 TC<sub>4</sub> could be investigated without calibrating the change in rotational brightness. Only seven images were obtained, due to the poor weather on October 10, 2017, with an exposure time of 120 s.

In addition, we observed 2012 TC<sub>4</sub> on October 10, 2017, using two 0.4 m  $f/10$  telescopes equipped with SBIG STL-1001E CCD ( $1024 \times 1024$  pixels) at Nayoro Observatory. The FoV of each telescope was around  $22' \times 22'$ . The goal was to obtain the color index in the visible wavelength region by simultaneously imaging with each telescope, using an IDAS R filter and a Johnson V filter. The exposure time for each telescope was 30 s. The color index could not be estimated due to the poor S/N; however the photometric data helped complement the phase of the lightcurve.

Finally, the 1.13 m  $f/9.7$  telescope at Anan Science Center provided the photometric data for lightcurve on October 11, 2017. The detector and FoV were the SBIG STX-16803 CCD ( $4096 \times 4096$  pixels) and  $11.''5 \times 11.''5$ , respectively. The photometry was conducted with an exposure time of 6 s by the  $2 \times 2$  binning mode without the use of a filter.

### 2.2. Data Reduction for Lightcurve

All images were bias and flat-field corrected. The observational time was corrected using the light-travel time from 2012 TC<sub>4</sub> to the observatory site. To calibrate the magnitude fluctuations due to the change of atmospheric conditions, a relative photometry was conducted using reference stars imaged in the same frame as 2012 TC<sub>4</sub>:

$$F_c^i(t) = F_0^i(t) - \overline{F_r^i(t)}, \quad (1)$$

where  $F_c^i(t)$  is the calibrated lightcurve of 2012 TC<sub>4</sub> under the  $i$ th observational condition, namely, each observatory, each observation day, and each filter.  $F_0^i(t)$  is the raw magnitude of 2012 TC<sub>4</sub>;  $\overline{F_r^i}(t)$  is the average raw magnitude of the reference stars and represents the change of atmospheric conditions;  $t$  is the observational time. There were 20-60 and three reference stars for Kiso Observatory and BSGC observations, respectively. One reference star was applied for the observations at Naylor Observatory and Anan Science Center. Next, offset magnitudes  $\Delta F^i$  were calculated to adjust the lightcurve of each observational condition. Here, we notes that the differences of the phase angle and the distances of 2012 TC<sub>4</sub> among the observational conditions are not regarded in the relative photometry. The offset magnitudes  $\Delta F^i$  was estimated as the difference of the average magnitude  $\overline{F_c^i}$  and the standard average magnitude  $\overline{F_c^{kiso10}}$ , obtained on October 10, 2017, at Kiso Observatory:

$$\Delta F^i = \overline{F_c^i} - \overline{F_c^{kiso10}}, \quad (2)$$

where the standard average magnitude  $\overline{F_c^{kiso10}}$  was estimated by comparing with the SDSS  $g'$  magnitude of reference stars. The standard average magnitude was 17.575 mag. Since the Tomo-e Gozen was not equipped with the SDSS  $g'$  filter, the standard average magnitude could be affected by a constant offset due to possible imperfect color correction. The constant offset was, however, estimated to be up to  $\sim 0.1$  mag, which has little impact on the following discussion. The calibration process above may introduce some systematic error in  $\Delta F^i$ , since each observation covered the different phase of the lightcurve and the average brightness should be different in the observational conditions. However, we presume that the systematic errors were sufficiently small, since the observation time of each observational condition was enough long compared with the rotational period as will be described later. We can safely use the average magnitude  $\overline{F_c^i}$  to adjust the lightcurves obtained in the different observational conditions. Finally, the lightcurve of 2012 TC<sub>4</sub>,  $F(t)$  could be described as

$$F(t) = F_c^i(t) + \Delta F^i. \quad (3)$$

### 2.3. Data Reduction for Multiband Photometry

The multiband photometry in the visible wavelength region was conducted in BSGC. We measured the flux of 17 standard stars from the SDSS Data Release 12 (Alam et al. 2015), whose stars were imaged simultaneously in the same frame as 2012 TC<sub>4</sub>. These objects have magnitudes of about 14-16 mag in the  $g'$ -band and classification code 1 (= primary), quality flag 3 (= good), and object class 6 (= star). The apparent magnitude of 2012 TC<sub>4</sub> was derived using the conversion factors that were evaluated from the 17 standard stars. Since 2012 TC<sub>4</sub> is fast-rotating, its brightness inevitably changes during the filter switch. We defined the time of recording the first  $g'$  images as a standard time (JD = 2458036.9707319), and then we calibrated an amount of brightness change for the standard time. The amount of brightness change was estimated by the fitting curve of the lightcurve as will be described in the following chapter. The multiband photometry in the near-infrared wavelength region was conducted at the Nishi-Harima Observatory. To increase the photometric accuracy, the seven obtained images were stacked with the median. The photometric standard star was one 2MASS catalog star (source designation: 22552054-0349375,  $J = 13.586 \pm 0.027$ ,  $H = 13.003 \pm 0.029$ ,  $K_s = 12.926 \pm 0.033$ ) that was imaged simultaneously with 2012 TC<sub>4</sub> in two of the seven frames.

## 3. RESULTS

### 3.1. Lightcurve

Assuming a double-peaked lightcurve, we carried out a periodicity analysis based on the Lomb-Scargle periodogram (Lomb 1976; Scargle 1982). We had a possibility to evaluate the inaccurate rotational period, due to the change in the geometric relationship between the Earth, 2012 TC<sub>4</sub>, and Sun for a few days. To avoid this, only the stable data obtained on October 10, 2017, at Kiso Observatory were used in the periodic analysis. The power spectrum from the periodogram showed a first period of  $12.25 \pm 0.01$  min and a second period of  $8.47 \pm 0.01$  min (Figure 1). The result was consistent with other observational results (Sonka et al. 2017; Warner 2018; Tan & Gao 2018)<sup>1</sup>. The appearance of two fast-rotating periods shows that 2012 TC<sub>4</sub> is a tumbling and monolithic asteroid. Substituting 12.25 min and 8.47 min into  $P_1$  and  $P_2$ , respectively, the period ratio  $P_1:P_2$  became approximately 13:9. In order to fit a curve to

<sup>1</sup> In addition, "The 2012 TC<sub>4</sub> Observing Campaign." <http://2012tc4.astro.umd.edu/index.shtml>

the lightcurve of a tumbling asteroid, “*Combined Period*”  $P_c$  was defined by

$$P_c = \frac{9P_1 + 13P_2}{2}. \quad (4)$$

The same surface of 2012 TC<sub>4</sub> faces the observer every  $P_c$  of 110.18 min. Next, we made the folded lightcurve with period of  $P_c$  for each day. The common specific features appear in the different phases of the folded lightcurve for each day. The folded lightcurve covering three observation days was obtained by matching the specific features in the phase (Figure 2). The obtained lightcurve was fitted to the two-dimensional Fourier series (Pravec et al. 2005):

$$\begin{aligned} F^m(t) = & C_0 + \sum_{j=1}^m \left[ C_{j0} \cos \frac{2\pi j}{P_1} t + S_{j0} \sin \frac{2\pi j}{P_1} t \right] \\ & + \sum_{k=1}^m \sum_{j=-m}^m \left[ C_{jk} \cos \left( \frac{2\pi j}{P_1} + \frac{2\pi k}{P_2} \right) t \right. \\ & \left. + S_{jk} \sin \left( \frac{2\pi j}{P_1} + \frac{2\pi k}{P_2} \right) t \right], \end{aligned} \quad (5)$$

where  $m$  is the order;  $C_0$  is the mean reduced light flux;  $C_{jk}$  and  $S_{jk}$  are the Fourier coefficients for the linear combination of the two frequency  $P_1^{-1}$  and  $P_2^{-1}$ , respectively; and  $t$  is the time. Substituting  $m = 4$ ,  $P_1 = 12.25$  min, and  $P_2 = 8.47$  min for 2012 TC<sub>4</sub>, a fitting curve was obtained, as shown by the blue lines in Figure 2. The  $C_0$  value was 17.578 mag. The brightness was around the same with the standard average magnitude of 17.575 mag described in Section 2.2. This indicates quantitatively that the offset error obtained in Eq. (2) is enough small for the purpose of obtaining the fitting curve. The top of Figure 2 shows that the obtained data can cover almost all phases in the lightcurve. The second top of Figure 2 indicates that the data of multiband photometry on BSGC is distributed evenly to the phase of the lightcurve. This means that the precise color index can be evaluated by stacking the data for each filter, assuming that 2012 TC<sub>4</sub> has a homogeneous surface. The graph legend “Kiso 11. Oct/1st” in the bottom of Figure 2 shows the result of zeroth-order photometry by grism spectroscopy. Thus, the photometric accuracy is slightly worse than the result of photometry in the graph legend “Kiso 11. Oct/2nd”. A precise and high time resolution lightcurve was successfully obtained in the graph legend “Kiso 11. Oct/2nd” by taking the advantage of a unique feature of the Tomo-e Gozen camera. The high time resolution lightcurve contributes to the drawing of a precise fitting curve.

### 3.2. Taxonomic Class and Diameter

The taxonomic class in the visible wavelength region is investigated in terms of a reflectance color gradient and a log reflectance spectrum (Carvano et al. 2010). The reflectance color gradient and log reflectance spectrum are deduced from the color indexes of 2012 TC<sub>4</sub>. Although the adequate wavelength calibration could not be carried out in grism spectroscopy at Kiso Observatory, the spectrum feature did not show the time variation. This indicated that 2012 TC<sub>4</sub> had a homogeneous surface and the color indexes did not also show the time variation. Assuming the homogeneous surface of 2012 TC<sub>4</sub>, the photometric accuracy could be increased by averaging the flux for each filter. The color indexes were  $g' - r' = 0.479 \pm 0.031$ ,  $r' - i' = 0.187 \pm 0.023$ , and  $i' - z' = 0.035 \pm 0.036$ , respectively. The reflectance color is defined as

$$C_{\lambda_j} = -2.5(\log_{10} R_{\lambda_j} - \log_{10} R_{\lambda_{ref}}), \quad (6)$$

where  $C_{\lambda_j}$  and  $R_{\lambda_j}$  are the reflectance color and the reflectance at a given wavelength;  $R_{\lambda_{ref}}$  is the reflectance at the reference wavelength; and the subscript  $j$  specifies the wavelength. The wavelengths of  $j = 1, 2, 3$ , and 4 correspond to the central wavelengths of the SDSS  $g'$  (0.477  $\mu\text{m}$ ),  $r'$  (0.623  $\mu\text{m}$ ),  $i'$  (0.763  $\mu\text{m}$ ), and  $z'$  (0.913  $\mu\text{m}$ ) filters, respectively. When we use the  $g'$  filter as the reference, the reflectance colors of the  $r'$  filter is calculated from the color index as

$$C_r = (r' - g') - C_{\odot rg}, \quad (7)$$

where  $C_{\odot rg}$  is the  $r' - g'$  color of the Sun. We adopted the solar colors  $C_{\odot rg}$ ,  $C_{\odot ig}$ , and  $C_{\odot zg}$  (Ivezić et al. 2001). The reflectance colors of the other filters were calculated in the same manner. The reflectance color gradient is defined as

$$\gamma_j = -0.4 \frac{C_{\lambda_{j+1}} - C_{\lambda_j}}{\lambda_{j+1} - \lambda_j}. \quad (8)$$



We deduced the reflectance color gradients of  $\gamma_g = 0.079 \pm 0.038$ ,  $\gamma_r = 0.249 \pm 0.043$ , and  $\gamma_i = -0.013 \pm 0.052$ . Figure 3 shows the reflectance color gradients of 2012 TC<sub>4</sub> and asteroids of major taxonomic classes. The rectangles in Figure 3 indicates the range of reflectance color gradients of C, X, D, L, S, A, Q, O, and V-type asteroids in the SDSS Moving Object Catalog (SDSS-MOC). The top, middle and bottom figures correspond to the  $\gamma_g$ ,  $\gamma_r$ , and  $\gamma_i$ , respectively. The thick horizontal lines are the average reflectance color gradients of 2012 TC<sub>4</sub>. The reflectance color gradients of 2012 TC<sub>4</sub> are consistent with the range of X-type asteroids. The log reflectance for 2012 TC<sub>4</sub> was normalized at the  $g'$  filter. The normalized log reflectance of the  $r'$ ,  $i'$ , and  $z'$  were  $1.01 \pm 0.01$ ,  $1.05 \pm 0.01$ , and  $1.04 \pm 0.02$ , respectively. Figure 4 shows the log reflectance spectra of 2012 TC<sub>4</sub> and the asteroids of the X-, S-, C-, and L-types. The log reflectance spectrum of 2012 TC<sub>4</sub> is similar to that of the X-type. Both observational results indicate that the taxonomic classes of 2012 TC<sub>4</sub> in the visible wavelength region is the X-type. Moreover, the color indexes in the near-infrared wavelength region were  $J - H = 0.226 \pm 0.041$  and  $H - K_s = 0.034 \pm 0.045$ . These values were included in the range of C-complex ( $J - H = 0.28 \pm 0.08$ ,  $H - K_s = 0.11 \pm 0.08$ ), S-complex ( $J - H = 0.37 \pm 0.12$ ,  $H - K_s = 0.04 \pm 0.08$ ), and X-complex ( $J - H = 0.31 \pm 0.12$ ,  $H - K_s = 0.14 \pm 0.07$ ) (Popescu et al. 2016). Therefore, the taxonomic class of 2012 TC<sub>4</sub> was concluded to be an X-type. The color indexes are summarized in Table 3.

We estimate the absolute magnitude  $H_V$  and effective diameter of 2012 TC<sub>4</sub>. The average apparent  $r'$  magnitude of 2012 TC<sub>4</sub> on October 10, 2017, at BSGC, was deduced to be  $17.129 \pm 0.017$  mag. The apparent  $V$  magnitude is described in the following form (Fukugita et al. 1996):

$$V = r' - 0.11 + 0.49 \left( \frac{(g' - r') + 0.23}{1.05} \right). \quad (9)$$

Here, for our photometric precision requirements, the difference between the AB magnitude and Vega magnitude in the  $V$  band is negligible. The reduced magnitude at the phase angle,  $\alpha$ , is expressed as  $H(\alpha) = V - 5 \log_{10}(R\Delta)$ , where  $R$  and  $\Delta$  are the heliocentric and geocentric distances in au, respectively. The absolute magnitude is expressed as a so-called  $H$ - $G$  function (Bowell et al. 1989):

$$H_V = H(\alpha) + 2.5 \log_{10}[(1 - G)\Phi_1(\alpha) + G\Phi_2(\alpha)], \quad (10)$$

where  $G$  is the slope parameter dependent on the asteroid's taxonomy. When we apply  $G = 0.20 \pm 0.09$  for X-types (Vereš et al. 2015),  $H_V$  becomes  $28.54 \pm 0.03$  mag. An effective diameter of asteroids  $D$  (in kilometer) is described as

$$D = 1329 \times 10^{-H_V/5} p_V^{-1/2}, \quad (11)$$

where  $p_V$  is the geometric albedo. Assuming an albedo of  $0.098 \pm 0.081$  for the X-type (Usui et al. 2013), the effective diameter and range were found to be 8 m and  $6 \text{ m} < D < 20 \text{ m}$ , respectively. Since Mainzer et al. (2011b) also showed the albedo of  $0.099 \pm 0.161$  for Tholen X-complex class and the albedo of  $0.111 \pm 0.143$  for Bus-DeMeo X-complex class, the assumption of  $\sim 0.1$  for the X-type albedo was reasonable. We should note, however, the X-complex includes the E-, M-, and P-types, whose albedos are  $0.454 \pm 0.119$ ,  $0.169 \pm 0.044$ , and  $0.063 \pm 0.017$ , respectively (Usui et al. 2013). The estimated diameter can be affected by the uncertainty of the albedo among the X-complex asteroids.

### 3.3. Shape and Rotational Motion

The period analysis revealed that 2012 TC<sub>4</sub> is a tumbling asteroid with a rotational period and precession period. However, period analysis alone cannot conclude whether a given period,  $P_1$  or  $P_2$ , corresponds to the rotational period or precession period. Thus, we make the shape and rotational motion models of 2012 TC<sub>4</sub>, which is recognized as a force-free asymmetric rigid body, from the dynamic analytical solution. Previous studies have described the equations of motion for a force-free asymmetric rigid body (Samarasinha & A'Hearn 1991; Kaasalainen 2001). The main equations used in this study are detailed in the Appendix. The shape and rotational motion models of 2012 TC<sub>4</sub> were made by substituting the observational result into the equations of this subsection and the Appendix. However, it should be noted that the shape and rotational motion models are representative examples, not unique solutions. Here, we define  $L_s$  (short axis length),  $L_i$  (intermediate axis length), and  $L_l$  (long axis length) when 2012 TC<sub>4</sub> is a triaxial ellipsoid body. The axes satisfy the relationship  $L_s < L_i < L_l$ . The rotational motions of asteroids are categorized into long axis modes (LAM) and short axis modes (SAM). The body of LAM rotates completely around the long axis ( $\psi$  in the Appendix) and oscillates around the short axis ( $\phi$  in the Appendix), as seen by an external observer. On the other hand, the body of SAM oscillates around the long axis ( $\psi$  in the Appendix) and rotates fully around the short

axis ( $\phi$  in the Appendix), as seen by an external observer. The shape and rotational motion models of 2012 TC<sub>4</sub> were made for LAM and SAM, respectively.

First, the LAM models were made. The relation between the lightcurve amplitude and phase angle is shown as follows:

$$A(0) = \frac{A(\alpha)}{1 + c\alpha}, \quad (12)$$

where  $A(\alpha)$  is the lightcurve amplitude at the phase angle,  $\alpha^\circ$ , and  $c$  is the photometric phase slope coefficient. Since the X-type of 2012 TC<sub>4</sub> includes the E-type, M-type, and P-type, 0.03 of the M-type (Zappalà et al 1990) was adopted as the  $c$  value. Assuming that the light-scattering cross-section of 2012 TC<sub>4</sub> is projected onto the plane of the sky, the lightcurve amplitude is described through the lower limit to the true cross-section ratio of the body as

$$A(0) = 2.5 \log_{10} \left( \frac{S_{max}}{S_{min}} \right), \quad (13)$$

where  $S_{max}$  and  $S_{min}$  are the maximum and minimum light-scattering cross-sections, respectively. The maximum amplitude of 2012 TC<sub>4</sub> is 1.434 mag and appears at a phase around 0.2 in Figure 2 when the phase angle is  $39^\circ$ . Therefore, the relationship  $L_l = 2.40L_s$  was obtained, assuming  $S_{max} = \pi L_l L_i$  and  $S_{min} = \pi L_i L_s$ . Alternatively, the relationship  $L_i = 2.40L_s$  could be obtained from  $S_{max} = \pi L_l L_i$  and  $S_{min} = \pi L_l L_s$ , when 2012 TC<sub>4</sub> almost simply rotates around the long axis and an observer sees 2012 TC<sub>4</sub> from the vertical direction for the total rotational angular momentum vector. As described above, period analysis alone is insufficient to determine whether  $P_1$  or  $P_2$  corresponds to  $P_\psi$  (period of  $\psi$ ) or  $P_\phi$  (period of  $\phi$ ) in the Appendix. Thus, there were four cases for the LAM models, whose combinations were  $L_l = 2.40L_s$  or  $L_i = 2.40L_s$  for  $P_\psi = 12.25$  min and  $P_\phi = 8.47$  min or  $P_\psi = 8.47$  min and  $P_\phi = 12.25$  min. Substituting the axial ratios and periods to Eq. (A11), the following limits of  $L_s$ ,  $L_i$ , and  $L_l$  could be taken for four cases:

- Case 1:  $L_l = 2.40L_s$ ,  $P_\psi = 12.25$  min,  $P_\phi = 8.47$  min,  $L_i \leq 1.88L_s$
- Case 2:  $L_i = 2.40L_s$ ,  $P_\psi = 12.25$  min,  $P_\phi = 8.47$  min,  $L_l \geq 2.97L_s$
- Case 3:  $L_l = 2.40L_s$ ,  $P_\psi = 8.47$  min,  $P_\phi = 12.25$  min,  $L_i \leq 1.39L_s$
- Case 4:  $L_i = 2.40L_s$ ,  $P_\psi = 8.47$  min,  $P_\phi = 12.25$  min,  $L_l \geq 3.69L_s$

The combination of the average rotational velocities were  $\bar{\phi} \sim 42.5 \text{ deg}\cdot\text{min}^{-1}$  and  $\bar{\psi} \sim 29.4 \text{ deg}\cdot\text{min}^{-1}$  or  $\bar{\phi} \sim 29.4 \text{ deg}\cdot\text{min}^{-1}$  and  $\bar{\psi} \sim 42.5 \text{ deg}\cdot\text{min}^{-1}$ . Moreover, we applied  $L_i = 8$  m as the effective diameter of 2012 TC<sub>4</sub>. In addition, the moments of inertia of Eq. (A4) were given using the total rotational angular momentum  $M$  and total rotational kinetic energy  $E$  as follows:

$$\frac{M^2}{2E} = \frac{(nI_l + I_i)}{n + 1} \quad \text{or} \quad \frac{(I_l + mI_i)}{m + 1}, \quad (14)$$

where  $n$  is an integer from 1 to 9 and  $m$  is an integer from 2 to 9. The tumbling status were roughly described by changing the integer  $n$  and  $m$ . The combination of the  $n$ ,  $m$ , and axial lengths that satisfies the observed velocities  $\bar{\phi}$  and  $\bar{\psi}$  was sought. The axial lengths were scanned in steps of 0.1 m for each case. The results were the following combinations:

- Case 1':  $(L_s, L_i, L_l) = (7.5 \text{ m}, 8.0 \text{ m}, 18.0 \text{ m})$ ,  $M^2/2E = (I_l + 3I_i)/4$
- Case 3':  $(L_s, L_i, L_l) = (6.2 \text{ m}, 8.0 \text{ m}, 14.9 \text{ m})$ ,  $M^2/2E = (8I_l + I_i)/9$
- Case 4':  $(L_s, L_i, L_l) = (3.3 \text{ m}, 8.0 \text{ m}, 14.3 \text{ m})$ ,  $M^2/2E = (2I_l + I_i)/3$

There was no solution that satisfied the observed velocities  $\bar{\phi}$  and  $\bar{\psi}$  for ‘‘Case 2’’.

Next, the SAM models were made. The relationship of  $L_l = 2.40L_s$  was obtained, assuming  $S_{max} = \pi L_l L_i$  and  $S_{min} = \pi L_i L_s$ . Alternatively, the relationship of  $L_l = 2.40L_i$  could be obtained from  $S_{max} = \pi L_l L_s$  and  $S_{min} = \pi L_i L_s$ , in the case that 2012 TC<sub>4</sub> almost simply rotates around the short axis and an observer sees 2012 TC<sub>4</sub> from the vertical direction for the total rotational angular momentum vector. The combination of the rotational period and precession period is limited to be  $P_\psi = 12.25$  min and  $P_\phi = 8.47$  min by Eq. (A20). Substituting the axial ratios and periods into Eq. (A19), the following limit of  $L_s$ ,  $L_i$ , and  $L_l$  could be taken for two cases:

- Case 5:  $L_l = 2.40L_s$ ,  $P_\psi = 12.25$  min,  $P_\phi = 8.47$  min,  $L_i \geq 2.29L_s$
- Case 6:  $L_l = 2.40L_i$ ,  $P_\psi = 12.25$  min,  $P_\phi = 8.47$  min,  $L_i \geq 1.81L_s$

The average rotational velocities were  $\bar{\phi} \sim 42.5 \text{ deg}\cdot\text{min}^{-1}$  and  $\bar{\psi} \sim 29.4 \text{ deg}\cdot\text{min}^{-1}$ . Moreover, we applied  $L_i = 8 \text{ m}$  as the effective diameter of 2012 TC<sub>4</sub>. In addition, the moments of inertia of Eq. (A12) were given as follows:

$$\frac{M^2}{2E} = \frac{(nI_s + I_i)}{n + 1} \quad \text{or} \quad \frac{(I_s + mI_i)}{m + 1}, \quad (15)$$

where  $n$  is an integer from 1 to 9 and  $m$  is an integer from 2 to 9. The tumbling status were roughly described by changing the integer  $n$  and  $m$ . The combination of the  $n$ ,  $m$ , and axial lengths that satisfies the observed velocities  $\bar{\phi}$  and  $\bar{\psi}$  was also sought. The axial lengths were scanned in steps of 0.1 m for each case. The result was the following combination:

•Case 6':  $(L_s, L_i, L_l) = (4.2 \text{ m}, 8.0 \text{ m}, 19.2 \text{ m})$ ,  $M^2/2E = (7I_l + I_i)/8$

There was no solution that satisfied the observed velocities  $\bar{\phi}$  and  $\bar{\psi}$  for “Case 5”.

Finally, the shape and rotational motion models (models 1, 3, 4, and 6) were made for four cases (Cases 1', 3', 4' and 6') using a commercial 3DCG (3-dimensional computer graphic) software, Shade 3D<sup>2</sup>, and selecting the plausible models using the artificial lightcurve produced by the shape and rotational motion models. The rendering models of 2012 TC<sub>4</sub> were drawn with the ray-tracing method in the software. The rotational motion was simplified with the fixed rotational velocities of  $\bar{\phi}$  and  $\bar{\psi}$ . The rendering models of 2012 TC<sub>4</sub> were read out in BMP format in steps of 0.1 mins. The artificial lightcurves were produced by the brightness change in the image of each rendering model. The artificial lightcurves are shown in Figure 5. The artificial lightcurves do not rigorously reflect the direction of rotational angular momentum or the detailed topography of 2012 TC<sub>4</sub>. However, the shapes of the lightcurves help to narrow down the plausible models. When the lightcurve in Figure 2 is compared to the artificial lightcurves of Figure 5, it can be seen that the artificial lightcurves of models 1 and 6 do not match the observed lightcurve, with respect to the unchanged lightcurve amplitude. On the other hand, it can be seen that the artificial lightcurves of models 3 and 4 created changes in the amplitude, like the observed lightcurve. Therefore, we concluded models 3 and 4 were the plausible models of 2012 TC<sub>4</sub>. For any case of models 3 and 4, the shape of 2012 TC<sub>4</sub> is flat and elongated like a pancake. As an example, the shape of model 4 is shown in Figure 6, and the time variation of rotational motion is shown in Figure 7. The rotational motion in model 3 is omitted, since the rotational motion of model 3 is similar to that of model 4. We summarize the shape and rotational motion models of 2012 TC<sub>4</sub> in Table 4. The average  $\theta$  value is around  $29.0 \text{ deg}$  and oscillates within the range of  $\pm 0.4 \text{ deg}$  in model 3. The average  $\dot{\phi}$  value is around  $29.4 \text{ deg}\cdot\text{min}^{-1}$  and oscillates within the range of  $\pm 1.5 \text{ deg}\cdot\text{min}^{-1}$  in model 3. The average  $\theta$  value is around  $48.5 \text{ deg}$  and oscillates within the range of  $\pm 1.5 \text{ deg}$  in model 4. The average  $\dot{\phi}$  value is around  $29.4 \text{ deg}\cdot\text{min}^{-1}$  and oscillates within the range of  $\pm 2.4 \text{ deg}\cdot\text{min}^{-1}$  in model 4. The  $\dot{\psi}$  is almost constant at around  $42.5 \text{ deg}\cdot\text{min}^{-1}$  for both models 3 and 4. The change of  $\psi$  is not obvious at the second row of Figure 7.

#### 4. DISCUSSION

We have found that 2012 TC<sub>4</sub> is a tumbling, fast-rotating, and monolithic asteroid. Discoveries of fast-rotating asteroid are increasing with asteroid surveys and follow-up observations (Pravec et al. 2000; Hergenrother & Whiteley 2011). The number of fast-rotating asteroids is 84 in the Lightcurve Database (LCDB) with “Quality = 3 (denotes a secure result with no ambiguity and full lightcurve coverage)” (Warner et al. 2009). Out of these, tumbling asteroids are 2000 WL<sub>107</sub> (Pravec et al. 2005), 2008 TC<sub>3</sub> (Betzler et al. 2009; Scheirich et al. 2010), 2004 FH (LCDB), 2013 SU<sub>24</sub> (Warner 2014; Benishek 2014), 2014 SC<sub>324</sub> (Warner 2015), 2015 VY<sub>105</sub> (Carbognani & Buzzi 2016), 2016 QS<sub>11</sub> (LCDB), 2018 AJ (Warner & Pravec 2018), and 2012 TC<sub>4</sub>. Moreover, only 2008 TC<sub>3</sub> had been revealed the three axis ratios. This study of 2012 TC<sub>4</sub> is a second sample to the elucidation of three axis ratios. We discuss the formation process of a tumbling and fast-rotating asteroid. The causes of a precession motion were proposed to be impact events with another object, planet encounters, and the decrease of rotational velocity due to the YORP effect (Pravec et al. 2005). The precession motion by the planet encounters works effectively for slow-rotating asteroids (Scheeres et al. 2004). Furthermore, fast-rotating asteroids do not start the precession motion due to the decrease of rotational velocity by the YORP effect. Therefore, the cause of precession motion for a tumbling and fast-rotating asteroid is an impact event with another object. Assuming an albedo of 0.2, the diameters of nine tumbling and fast-rotating asteroids, including that of 2012 TC<sub>4</sub>, are smaller than 41 m in diameter. The small diameter indicates that the nine tumbling

<sup>2</sup> Shade 3D is produced by Shade3D Co., Ltd. <https://shade3d.jp/en/>



and fast-rotating asteroids would be ejected objects by the impact event rather than the impacted parent objects. Michikami et al. (2010) pointed out that the axial ratio of the intermediate axis to the long axis of fast-rotating asteroids (diameter < 200 m and rotational period < 1 h) is similar to that of ejecta in laboratory impact experiments and that of boulders on Itokawa and Eros. For example,  $L_i/L_l$ , the mean value of axial ratios of boulders larger than 5 m on Itokawa is  $0.61 \pm 0.19$ . Since the lightcurve amplitudes of nine tumbling asteroids are larger than 1.0 mag, the shape of nine tumbling asteroids presumably indicates elongated boulder-like shapes. In particular, the axial ratio  $L_i/L_l$  of 2012 TC<sub>4</sub> is 0.54 in model 3 and 0.56 in model 4, and the axial ratio  $L_i/L_l$  of 2008 TC<sub>3</sub> is 0.54. The NEOs, 2012 TC<sub>4</sub> and 2008 TC<sub>3</sub>, will be objects similar to the boulders on Itokawa. Furthermore, we discuss how the impact event happened to fast-rotating asteroids using the axis ratio,  $L_s/L_l$ . The collisional destruction process is divided into impact cratering (low impact energy) and catastrophic disruption (high impact energy). Laboratory impact experiments demonstrated that  $L_s/L_l$  of impact cratering fragments is  $\sim 0.2$ ,  $L_s/L_l$  of catastrophic disruption fragments is  $\sim 0.5$ , and  $L_s/L_l$  decreases with decreasing impact energy (Michikami et al. 2016). Numerous impact fragments were generated by the laboratory impact experiments. Despite of the catastrophic disruption, a part of the impact fragments will indicate low  $L_s/L_l$ . Thus, the collisional destruction process cannot be immediately concluded from the  $L_s/L_l$  of asteroids. Nonetheless, the axial ratio  $L_s/L_l$  of 2012 TC<sub>4</sub> is 0.42 in model 3 and 0.23 in model 4, and the axial ratio  $L_s/L_l$  of 2008 TC<sub>3</sub> is 0.36. The NEO 2012 TC<sub>4</sub> could be generated by catastrophic disruption in model 3, and by impact cratering in model 4. The NEO 2008 TC<sub>3</sub> could have experienced the impact energy between models 3 and 4.

As we discussed above, 2012 TC<sub>4</sub> had possibly experienced an impact event. Here, we estimate the excitation and damping timescales of 2012 TC<sub>4</sub>. The excitation timescale, especially, helps to deduce the time of the impact event of 2012 TC<sub>4</sub>. An nutation angle ( $\theta$  in the Appendix) of asteroids with the LAM increases with dissipating the internal energy. Then, the motion of the asteroid transitions to the SAM via an unstable and temporary rotation mode around the intermediate axis. After the transition to the SAM, the nutation angle decreases with the time, and the SAM transitions to the pure rotation around the short axis, which is in alignment with the principal axis of moment of inertia. We call the transition time from the LAM to the SAM “excitation timescale”, and the transition time from the SAM to the pure rotation “damping timescale”. The excitation and damping timescale (Sharma et al. 2005, Breiter et al. 2012) are expressed as

$$T_s = D_s(h_1, h_2) \frac{\mu Q}{a^2 \rho \tilde{\omega}_s^3}, \quad (16)$$

where  $D_s(h_1, h_2)$  is a shape parameter;  $\mu$  is the elastic modulus;  $Q$  is the quality factor;  $\rho$  is the density;  $a$  is the half of the long axis length; and  $\tilde{\omega}_s$  is a representative angular velocity around the focusing principal axis. The quantities for the LAM have the subscript  $s = 1$ , and those for the SAM have the subscript  $s = 3$ . The shape parameter  $D_s(h_1, h_2)$  for the LAM and SAM are defined as

$$D_1(h_1, h_2) = \left[ \frac{h_1^2(1-h_1^2)(1+h_2^2)}{5(1+h_1^2h_2^2)} \right] \int_{\theta_1^0}^{\theta_1'} \frac{\sin\theta_1 \cos\theta_1}{\Psi_1} d\theta_1, \quad (17)$$

and

$$D_3(h_1, h_2) = - \left[ \frac{h_1^2(1+h_1^2)(1-h_2^2)}{5(1+h_1^2h_2^2)} \right] \int_{\theta_3^0}^{\theta_3'} \frac{\sin\theta_3 \cos\theta_3}{\Psi_3} d\theta_3, \quad (18)$$

where  $\theta_s^0$  and  $\theta_s'$  are the initial and the final maximum wobbling angle, respectively,  $h_1 \equiv L_i/L_l$ ,  $h_2 \equiv L_s/L_i$ ,  $\Psi_1$  and  $\Psi_3$  are dimensionless factor of the energy loss rate (Breiter et al. 2012). According to the manner of Pravec et al. 2014,  $\tilde{\omega}_1$  and  $\tilde{\omega}_3$  are represented as

$$\tilde{\omega}_1 = \frac{I_i}{I_s} \tilde{\omega}_2 \equiv \frac{1+h_1^2h_2^2}{h_1^2(1+h_2^2)} \tilde{\omega}_2, \quad (19)$$

and

$$\tilde{\omega}_3 = \frac{I_i}{I_l} \tilde{\omega}_2 \equiv \frac{1+h_1^2h_2^2}{1+h_1^2} \tilde{\omega}_2, \quad (20)$$

where  $I_s$ ,  $I_i$ , and  $I_l$  are the moment of inertias defined in the Appendix. When we use  $\tilde{\omega}_{obs} \equiv 2\pi/P_\phi$  as a proxy for  $\tilde{\omega}_2$  and  $a \equiv D_m/2h_1$ , where  $D_m$  is the asteroid mean diameter, the final formulae for the excitation and damping timescales become

$$T_1 = D_1(h_1, h_2) \frac{(h_1^2(1+h_2^2))^3 h_1^2 \mu Q P_\phi^3}{(1+h_1^2h_2^2)^3 2\pi^3 \rho D_m^2}, \quad (21)$$

and

$$T_3 = D_3(h_1, h_2) \frac{(1 + h_1^2)^3 h_1^2 \mu Q P_\phi^3}{(1 + h_1^2 h_2^2)^3 2\pi^3 \rho D_m^2}. \quad (22)$$

We adopted  $D_m = 8$  m,  $\mu = 10^9$  Pa,  $Q = 100$ , and  $\rho = 3000$  kg m<sup>-3</sup> for 2012 TC<sub>4</sub>. The typical timescale from the impact event to the status of model 3 became  $3.1 \times 10^5$  yr when the integration interval of  $\theta_1$  was from 0.1 *deg* to 29.0 *deg* in Eq. (17). The status of model 3 transitions to the SAM in the timescale of  $2.7 \times 10^5$  yr when the integration interval of  $\theta_1$  was from 29.0 *deg* to 89.9 *deg* in Eq. (17). After the transition to the SAM, the damping timescale,  $T_3$  became  $1.5 \times 10^7$  yr when the integration interval of  $\theta_3$  was from 89.9 *deg* to 0.1 *deg* in Eq. (18). In the same way, the typical timescale from the impact event to the status of model 4 became  $3.2 \times 10^5$  yr when the integration interval of  $\theta_1$  was from 0.1 *deg* to 48.5 *deg*. The status of model 4 transitions to the SAM in the timescale of  $1.8 \times 10^5$  yr when the integration interval of  $\theta_1$  was from 48.5 *deg* to 89.9 *deg*. The damping timescale,  $T_3$  became  $3.8 \times 10^7$  yr when the integration interval of  $\theta_3$  was from 89.9 *deg* to 0.1 *deg*. On the basis of the excitation and damping timescales, we can make the following scenario of 2012 TC<sub>4</sub>. Zappalà et al (2002), Morbidelli & Vokrouhlický (2003), and Granvik et al. (2017) described that impact events and dynamical mechanisms like the Yarkovsky effect continuously supply asteroids to the transportation resonances in the asteroid Main Belt. If asteroids once move into the transportation resonances, the orbit dynamically evolves to the NEO region in less than a million years (Morbidelli et al. 2002). After the migration to the NEO region, the dynamical lifetime of a 10 m-sized NEO is typically a few million years. In the case of 2012 TC<sub>4</sub>, its parent object had experienced an impact event in the asteroid Main Belt within  $\sim 3 \times 10^5$  yr and the ejected 2012 TC<sub>4</sub> dynamically evolved to the NEO region via the transportation resonances. Even if the derived  $\theta$  values was underestimated, the ongoing LAM of 2012 TC<sub>4</sub> is an evidence that the impact even should have happened less than  $\sim 6 \times 10^5$  yr ago. The result suggests that 2012 TC<sub>4</sub> should have a fresh surface, since 2012 TC<sub>4</sub> is not exposed to space weathering for more than  $\sim 6 \times 10^5$  yr. The motion of 2012 TC<sub>4</sub> will transition to the SAM in  $\sim 3 \times 10^5$  yr and then will reach the dynamical lifetime of the 10-m sized NEOs before the damping timescale of tens of million year elapses.

## 5. SUMMARY

We investigated the physical properties of 2012 TC<sub>4</sub> by visible and near-infrared photometry. We succeeded in obtaining unprecedented high time resolution lightcurve with the Tomo-e Gozen camera. The two fast-rotating periods showed that 2012 TC<sub>4</sub> is a tumbling and monolithic asteroid. The observations demonstrated the Tomo-e Gozen camera to be an extremely suitable instrument to observe fast-rotating and fast-moving asteroids. The multiband photometry indicated the taxonomic class of 2012 TC<sub>4</sub> to be an X-type. Assuming the typical albedo of the X-type asteroids, the diameter of 8 m and range of 6-20 m were deduced. Moreover, the shape and rotational motion models of 2012 TC<sub>4</sub> were estimated. The plausible models indicated that 2012 TC<sub>4</sub> has the rotational period of 8.47 min and precession period of 12.25 min with the LAM mode. The three axial lengths were  $6.2 \times 8.0 \times 14.9$  m or  $3.3 \times 8.0 \times 14.3$  m. In any model, the shape of 2012 TC<sub>4</sub> is flattened and elongated like a pancake, which suggests that 2012 TC<sub>4</sub> was produced by a past impact event. We also estimated the excitation and damping timescales. The excitation timescale implies that the impact event happened within  $\sim 3 \times 10^5$  yr and 2012 TC<sub>4</sub> has a fresh surface that has not been strongly influenced by the space weathering.

This study is a detailed observation of 10 m-sized small NEOs, following the study of 2008 TC<sub>3</sub>. Although the impact of a 10 m-sized NEO dose not cause a catastrophic disaster, the impact happens with a high probability from once a century to once in several decades (Torcarico 2017; Trilling 2017). It will become a crisis close to the Chelyabinsk meteor event (Popova et al. 2013). Furthermore, future space explorations plan to use 10 m-sized NEOs as resources. Thus, clarifying the physical properties of 10 m-sized NEOs is important for both planetary defense and future space exploration.

## APPENDIX

## A. MOTION OF FORCE-FREE RIGID BODY

The shape of an asteroid is approximated by a triaxial ellipsoid with the axial lengths  $L_s$ ,  $L_i$ , and  $L_l$ . The tumbling motion are divided into two classes: the long axis mode (LAM) and short axis mode (SAM). Here, the moment of inertia per unit mass for each axis can be described as

$$I_l = \frac{1}{20}(L_i^2 + L_s^2), \quad (\text{A1})$$

$$I_i = \frac{1}{20}(L_l^2 + L_s^2), \quad (\text{A2})$$

and

$$I_s = \frac{1}{20}(L_l^2 + L_i^2). \quad (\text{A3})$$

The motion for LAM can be expressed in terms of the total rotational angular momentum  $M$  and total rotational energy  $E$  as

$$I_l \leq \frac{M^2}{2E} < I_i. \quad (\text{A4})$$

The body approaches pure rotation about the long axis as  $M^2/2E$  approaches  $I_l$ . A new independent variable of time  $\tau$  and a constant of the motion  $k^2 (\leq 1)$  are defined by

$$\tau = t \sqrt{\frac{2E(I_i - I_l) \left( I_s - \frac{M^2}{2E} \right)}{I_l I_i I_s}}, \quad (\text{A5})$$

and

$$k^2 = \frac{(I_s - I_i) \left( \frac{M^2}{2E} - I_l \right)}{(I_i - I_l) \left( I_s - \frac{M^2}{2E} \right)}. \quad (\text{A6})$$

The motion of a triaxial ellipsoid can be described as the time-series change of Euler angles  $\psi$ ,  $\phi$ , and  $\theta$ . In the case of LAM,  $\psi$  is the rotation about the long axis;  $\phi$  is the precession about the total rotational angular momentum vector;  $\theta$  is the angle between the long axis and total rotational angular momentum vector  $M$ .  $\psi$ ,  $\theta$  and  $\dot{\phi}$  are described as

$$\psi = \text{atan2} \left( \sqrt{\frac{I_i}{I_i - I_l}} \text{sn}\tau, \sqrt{\frac{I_s}{I_s - I_l}} \text{cn}\tau \right), \quad (\text{A7})$$

$$\theta = \cos^{-1} \left( \text{dn}\tau \sqrt{\frac{I_l \left( I_s - \frac{M^2}{2E} \right)}{\frac{M^2}{2E} (I_s - I_l)}} \right), \quad (\text{A8})$$

and

$$\dot{\phi} = M \left[ \frac{(I_i - I_l) + (I_s - I_i) \text{sn}^2\tau}{I_s (I_i - I_l) + I_l (I_s - I_i) \text{sn}^2\tau} \right]. \quad (\text{A9})$$

Here,  $\text{sn}\tau$ ,  $\text{cn}\tau$  and  $\text{dn}\tau$  are Jacobian elliptic functions. In addition, the following relational expressions are established:

$$P_\psi = 4 \sqrt{\frac{I_l I_i I_s}{2E(I_i - I_l) \left( I_s - \frac{M^2}{2E} \right)}} \int_0^{\frac{\pi}{2}} \frac{du}{\sqrt{1 - k^2 \sin^2 u}}, \quad (\text{A10})$$

and

$$\frac{P_\psi}{P_\phi} \geq \sqrt{\frac{(L_l^2 + L_i^2)(L_l^2 + L_s^2)}{(L_l^2 - L_i^2)(L_l^2 - L_s^2)}} - 1. \quad (\text{A11})$$

The integral part of (A10) is the complete elliptic integral of the first kind.

On the other hand, the motion for SAM can be expressed as

$$I_i < \frac{M^2}{2E} \leq I_s. \quad (\text{A12})$$

The body approaches pure rotation about the short axis as  $M^2/2E$  approaches  $I_s$ . A new independent variable of time  $\tau$  and a constant of the motion  $k^2 (\leq 1)$  are defined by

$$\tau = t \sqrt{\frac{2E(I_s - I_i) \left( \frac{M^2}{2E} - I_l \right)}{I_l I_i I_s}}, \quad (\text{A13})$$

and

$$k^2 = \frac{(I_i - I_l) \left( I_s - \frac{M^2}{2E} \right)}{(I_s - I_i) \left( \frac{M^2}{2E} - I_l \right)}. \quad (\text{A14})$$

In the case of SAM,  $\phi$  is the rotation about the short axis;  $\psi$  is the oscillation about the long axis;  $\theta$  is the angle between the long axis and total rotational angular momentum vector  $M$ .  $\psi$ ,  $\theta$ , and  $\dot{\phi}$  are described as

$$\psi = \text{atan2} \left( \sqrt{\frac{I_i \left( I_s - \frac{M^2}{2E} \right)}{I_s - I_i}} \text{sn}\tau, \sqrt{\frac{I_s \left( \frac{M^2}{2E} - I_l \right)}{I_s - I_l}} \text{dn}\tau \right), \quad (\text{A15})$$

$$\theta = \cos^{-1} \left( \text{cn}\tau \sqrt{\frac{I_l \left( I_s - \frac{M^2}{2E} \right)}{\frac{M^2}{2E} (I_s - I_l)}} \right), \quad (\text{A16})$$

and

$$\dot{\phi} = M \left( \frac{\left( \frac{M^2}{2E} - I_l \right) + \left( I_s - \frac{M^2}{2E} \right) \text{sn}^2\tau}{I_s \left( \frac{M^2}{2E} - I_l \right) + I_l \left( I_s - \frac{M^2}{2E} \right) \text{sn}^2\tau} \right). \quad (\text{A17})$$

In addition, the following relational expressions are established:

$$P_\psi = 4 \sqrt{\frac{I_l I_i I_s}{2E(I_s - I_i) \left( \frac{M^2}{2E} - I_l \right)}} \int_0^{\frac{\pi}{2}} \frac{du}{\sqrt{1 - k^2 \sin^2 u}}. \quad (\text{A18})$$

The integral part of (A18) is the complete elliptic integral of the first kind. Moreover, the rotational period  $P_\phi$  has the following relationships with the oscillation period  $P_\psi$ :

$$\frac{P_\psi}{P_\phi} \geq \sqrt{\frac{(L_l^2 + L_s^2)(L_i^2 + L_s^2)}{(L_l^2 - L_s^2)(L_i^2 - L_s^2)}}, \quad (\text{A19})$$

and

$$\frac{P_\psi}{P_\phi} > 1. \quad (\text{A20})$$

**Table 1.** Observation states

Observation start and end time <sup>a</sup> (JD-2458000)	Exp.time (s)	Filter	Observatory	Average SNR <sup>b</sup>
35.9578326 – 35.9982278	10	--	Kiso (1.05 m)	~12
36.9028528 – 36.9888035	30	<i>V, R</i>	Nayoro (0.4 m)	<i>V</i> and <i>R</i> (~5)
36.90450 – 36.91530	120	<i>J, H, K<sub>s</sub></i>	Nishi-Harima (2.0 m)	<i>J</i> (~120) <i>H</i> (~240) <i>K<sub>s</sub></i> (~160)
36.9707319 – 37.1452383	60	<i>g', r', i', z'</i>	BSGC (1.0 m)	<i>g'</i> (~19) <i>r'</i> (~30) <i>i'</i> (~34) <i>z'</i> (~20)
37.0073257 – 37.0808347	10 5	--	Kiso (1.05 m)	~26
37.9282507 – 37.9375688	5	<i>grism</i>	Kiso (1.05 m)	~8
37.9390568 – 38.0126750	2	--	Kiso (1.05 m)	~66
38.0826590 – 38.1130069	6	--	Anan (1.13 m)	~7

<sup>a</sup>Center of exposure time. The time is calibrated light-travel time, with the exception of Nishi-Harima.

<sup>b</sup>SNR of Nishi-Harima is estimated by a image of seven stacked frame.

**Table 2.** Status of 2012 TC<sub>4</sub> each day

Year/mon/day (UT)	$\Delta^a$ (AU)	$\alpha^b$ ( $^\circ$ )	Sky motion "/min
2017/10/9.4578 – 9.4998	0.011 – 0.010	31.4 – 31.5	4.16 – 4.54
2017/10/10.4029 – 10.5808	0.007 – 0.0064	33.3 – 34.1	6.77 – 9.36
2017/10/11.4283 – 11.6130	0.0032 – 0.0025	38.0 – 40.7	28.17 – 43.24

<sup>a</sup>2012 TC<sub>4</sub> to observer distance.

<sup>b</sup>Phase angle (Sun-2012 TC<sub>4</sub>-observer).

**Table 3.** Color indexes of 2012 TC<sub>4</sub>.

Column	Values
<i>g</i> – <i>r'</i>	0.479 ± 0.031
<i>r'</i> – <i>i'</i>	0.187 ± 0.023
<i>i'</i> – <i>z'</i>	0.035 ± 0.036
<i>J</i> – <i>H</i>	0.226 ± 0.041
<i>H</i> – <i>K<sub>s</sub></i>	0.034 ± 0.045



**Table 4.** Shape and rotational motion models of 2012 TC<sub>4</sub>.

Column	Values
$L_s$	6.2 <i>m</i> (model 3), 3.3 <i>m</i> (model 4)
$L_i$	8.0 <i>m</i> (model 3 and model 4)
$L_l$	14.9 <i>m</i> (model 3), 14.3 <i>m</i> (model 4)
$P_\psi$	8.47 ± 0.01 <i>min</i>
$P_\phi$	12.25 ± 0.01 <i>min</i>
$\bar{\theta}$	29.0 <i>deg</i> (model 3), 48.5 <i>deg</i> (model4)
$\dot{\phi}$	29.4 <i>deg·min</i> <sup>-1</sup> (model 3 and 4)
$\dot{\psi}$	42.5 <i>deg·min</i> <sup>-1</sup> (model 3 and 4)

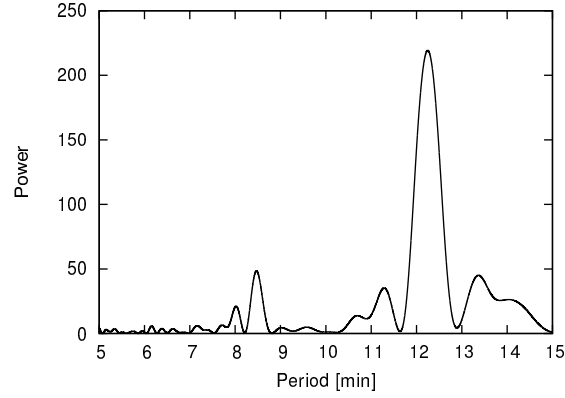


**Figure 1.** Power spectrum for the sidereal rotational period of 2012 TC<sub>4</sub>, assuming the double-peak lightcurve. The calculation is carried out by the data obtained on October 10, 2017, at Kiso Observatory.

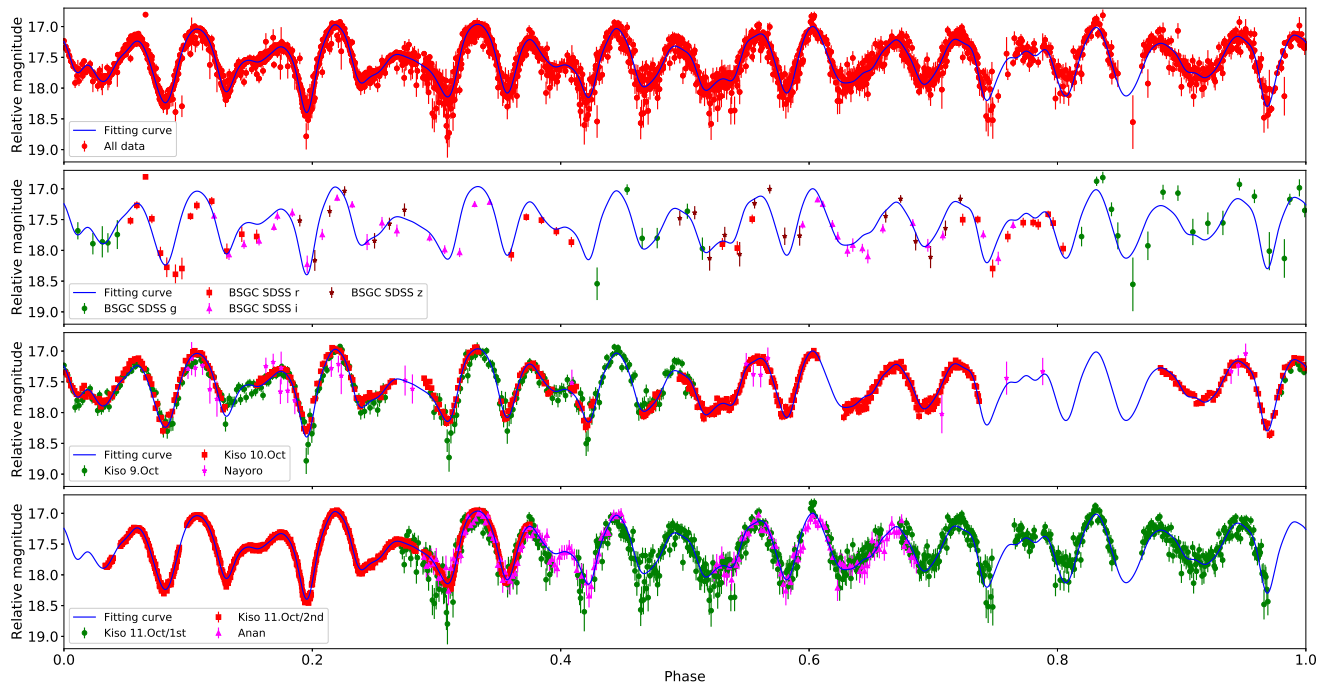


**Figure 2.** Lightcurve of 2012 TC<sub>4</sub>. As a result of motion analysis, we deduce the rotational period is  $8.47 \pm 0.01$  min and the precession period is  $12.25 \pm 0.01$  min. The phase in the figure indicates the complex period of 110.18 min. The relative magnitude corresponds to the apparent magnitude on October 10, 2017, at Kiso Observatory. Although the apparent magnitude is estimated by comparing the SDSS  $g'$  magnitude of reference stars, the Tomo-e Gozen is not equipped with the same filter. Therefore, the apparent magnitude is a relative magnitude in a precise sense. (Top) All data and the fitting curve. (2nd row) The timing of the multiband photometry on BSGC. The offset magnitude to the  $C_0$  for  $g'$ ,  $r'$ ,  $i'$ , and  $z'$  are -0.03 mag, 0.449 mag, 0.636 mag, and 0.674 mag, respectively.

(3rd row) The data on October 9 and 10, 2017, at Kiso Observatory. (Bottom) The data on October 11, 2017, at Kiso Observatory and Anan Science Center. The graph legend of “Kiso 11.Oct/1st” is the photometry of the zeroth-order data of grism spectroscopy. The graph legend of “Kiso 11.Oct/2nd” shows that the Tomo-e Gozen can obtain a precise and high time resolution lightcurve.

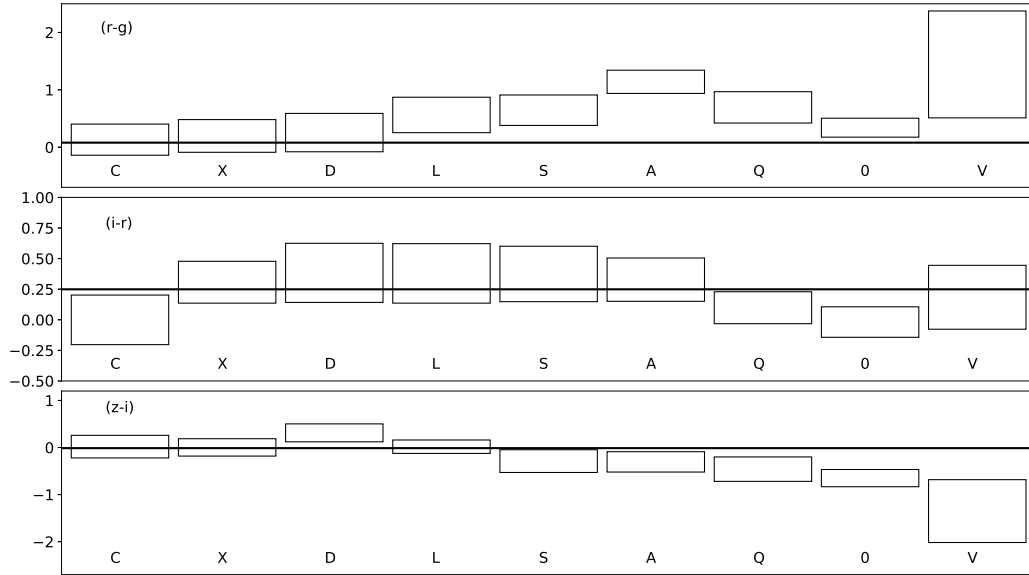


**Figure 3.** Reflectance color gradients of 2012 TC<sub>4</sub> and asteroids of major taxonomic classes. The rectangles indicate the range of reflectance color gradients of C, X, D, L, S, A, Q, O, and V-type asteroids in the SDSS Moving Object Catalog (SDSS-MOC). The top, middle and bottom figures correspond to the  $\gamma_g$ ,  $\gamma_r$ , and  $\gamma_i$ , respectively. The thick horizontal lines are the average reflectance color gradients of 2012 TC<sub>4</sub>. The reflectance color gradients of 2012 TC<sub>4</sub> are consistent with the range of X-type asteroids.

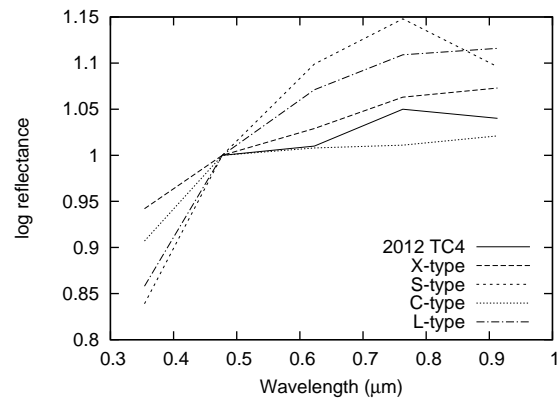


**Figure 4.** The log reflectance spectra of 2012 TC<sub>4</sub> and the asteroids of the X-, S-, C-, and L-types. The data in  $u'$  filter is not obtained for 2012 TC<sub>4</sub>.

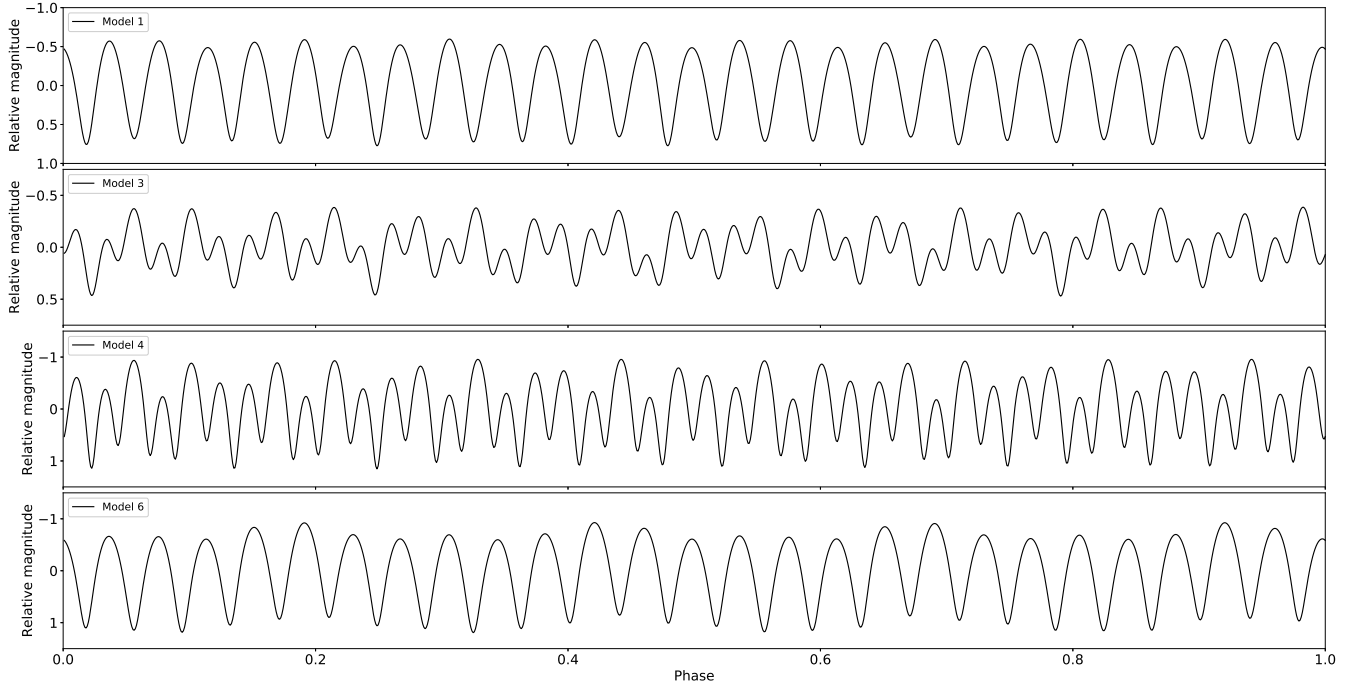
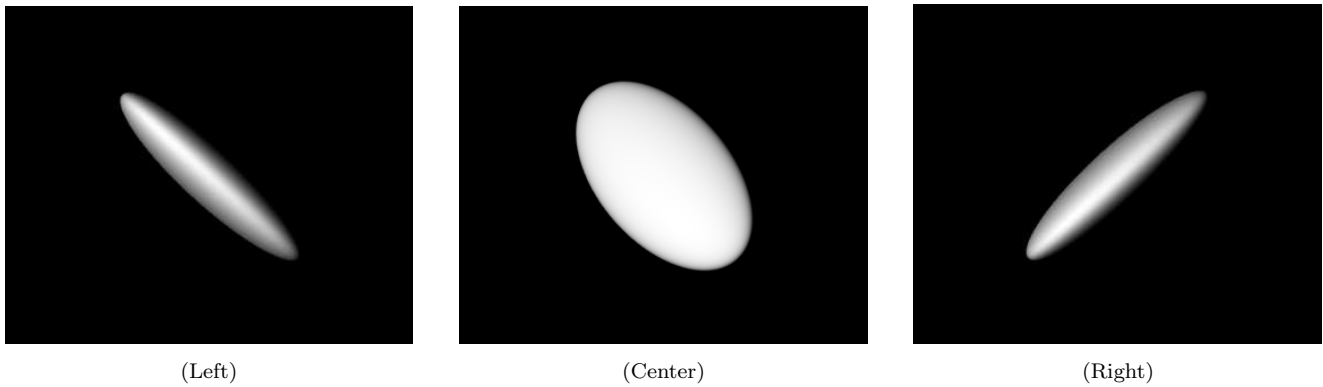


**Figure 5.** Artificial lightcurves of 2012 TC<sub>4</sub> in models 1, 3, 4, and 6.



(Left)

(Center)

(Right)

**Figure 6.** Shape of 2012 TC<sub>4</sub> for a model 4. An observer locates in the direction of the intermediate axis in the left figure. (Left) A view on phase 0 in Figure 5. (Center) A view on phase  $\sim 0.1$  in Figure 5. (Right) A view on phase  $\sim 0.5$  in Figure 5. An animated version of this figure is available in [http://www.spaceguard.or.jp/RSGC/TC4/TC4\\_LAM\\_4.mp4](http://www.spaceguard.or.jp/RSGC/TC4/TC4_LAM_4.mp4)

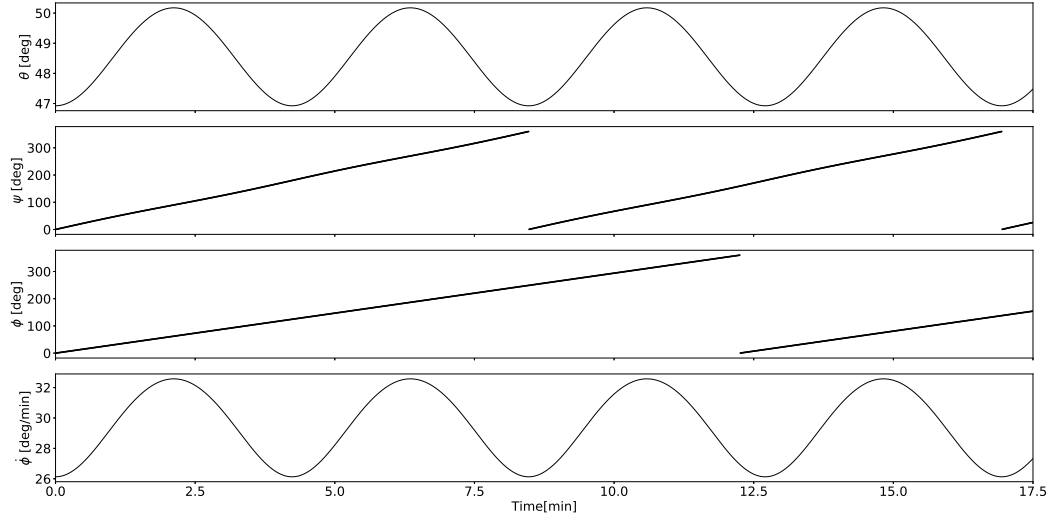


**Figure 7.** The Euler angle of  $\theta$ ,  $\phi$ , and  $\psi$  as a function of time for a model 4. This figure style is developed by [Samarasinha & A’Hearn \(1991\)](#). The angle  $\theta$  is the angle between the long axis and total rotational angular momentum vector  $M$ . The angle  $\phi$  and  $\psi$  measures the amount of precession executed by the long axis around  $M$  and amount of rotation around the long axis itself. For model 4, the axial lengths of  $3.3 \times 8.0 \times 14.3$  m were used with  $M^2/2E = (2I_l + I_i)/3$ . The nutation period,  $P_\theta$ , is exactly half the rotational period,  $P_\psi$ . The variation in the angular velocity,  $\dot{\psi}$ , is undetectable in plots of  $\psi$  vs time because the amplitude of variation is negligible. The angle  $\phi$  is described based on the constant of  $\dot{\phi} \sim 29.4$  minutes<sup>-1</sup>.



This research is supported in part by Japan Society for the Promotion of Science (JSPS) Grants-in-Aid for Scientific Research (KAKENHI) Grant Number 16K05310, JP18H01261, JP26247074, JP16H02158, JP16H06341, JP2905, 18H04575, JP18H01272, JP18K13599, and JSPS Program for Advancing Strategic International Networks to Accelerate the Circulation of Talented Researchers Grant Number JR2603. This research is also supported in part by Japan Science and Technology Agency (JST) Precursory Research for Embryonic Science and Technology (PRESTO), Research Center for the Early Universe (RESCEU), School of Science, the University of Tokyo, and the Optical and Near-infrared Astronomy Inter-University Cooperation Program.

## REFERENCES

- Abell, P. A., Barbee, B. W., Chodas, B. W., et al. 2016, in Asteroid IV, eds. P. Michel, F. E. DeMeo, & W. F. Bottke. (Tucson, AZ: Univ. Arizona Press), 855
- Alam, S., Albareti, F. D., Allende, P., et al. 2015, *ApJS*, 219, 12
- Benishek, V., 2014, *The Minor Planet Bulletin*, 41, 257
- Betzler, A. S., Novaes, A. B., Beltrame, P., et al. 2009, *The Minor Planet Bulletin*, 36, 58
- Bowell, E., Hapke, B., Domingue, D., et al. 1989, in Asteroids II, ed. R. P. Binzel et al. (Tucson: Univ. Arizona Press), 524
- Breiter, S., Rožek, A., & Vokrouhlický, D. 2012, *MNRAS*, 427, 755
- Carbognani, A., & Buzzi, L. 2016, *The Minor Planet Bulletin*, 43, 115
- Carvano, J. M., Hasselmann, P. H., Lazzaro, D., & Mothé-Diniz, T. 2010, *A&A*, 510, A43
- Chambers, K., & Pan-STARRS Team. 2016, *AAS Meeting Abstracts*, 227, 324.07
- Cheng, A. F., Rivikin, A. S., Michel, P., et al. 2018, *P&SS*, 157, 104
- Christensen, E., Lister, T., Larson, S., et al. 2014, in Asteroids, Comets, Meteors –Book of Abstracts, ed. K. Muinonen et al. (Finland: Helsinki), 97
- Fujiwara, A., Kawaguchi, J., Yeomans, D. K., et al. 2006, *Science*, 312, 1330
- Fukugita, M., Ichikawa, T., Gunn, J. E., et al. 1996, *AJ*, 111, 1748
- Granvik, M., Morbidelli, A., Vokrouhlický, D., et al. 2017, *A&A*, 698, 52
- Hergenrother, C. W., & Whiteley, R. J. 2011, *Icarus*, 214, 194
- Ishiguro, M., Kuroda, D., Hasegawa, S., et al. 2014, *ApJ*, 792, 74
- Ivezić, Ž., Tabachnik, S., Rafikov, R., et al. 2001, *AJ*, 122, 2749
- Kaasalainen, M. 2001, *A&A*, 376, 302
- Kaasalainen, M., Kwiatkowski, T., Abe, M., et al. 2003, *A&A*, 405, L29
- Kim, M-J., Choi, Y-J., Moon, H-K., et al. 2013, *A&A*, 550, 11
- Larson, S., Brownlee, J., Hergenrother, C., & Spahr, T. 1998, *BAAS*, 30, 1037
- Lomb, N. R. 1976, *Ap&SS*, 39, 447
- Mainzer, A., Bauer, J., Gray, T., et al. 2011a, *ApJ*, 731, 53
- Mainzer, A., Grav, T., Masiero, J., et al. 2011b, *ApJ*, 741, 90
- Mainzer, A., & NEOCam Science Team 2017, *American Astronomical Society, DPS meeting #49*, 219.01
- Michikami, T., Nakamura, A. M., Hirata, N., 2010, *Icarus*, 207, 277
- Michikami, T., Hagermann, A., Kadokawa, T., et al. 2016, *Icarus*, 264, 316
- Morbidelli, A., Bottke, W. F. Jr., Froeschl'e, Ch., Michel, P. 2002, in Asteroids III, ed. W. F. Bottke Jr et al. (Tucson: Univ. Arizona Press), 409
- Morbidelli, A., Vokrouhlický, D. 2003, *Icarus*163, 120
- Müller, T. G., Ďurech, J., Ishiguro, M., et al. 2017, *A&A*, 599, 103
- Ostro, S. J., Benner, L. A., Magri, C., et al. 2005, *M&PS* 40, 1563
- Polishook, D. 2013, *The Minor planet Bulletin*, 40, 42
- Popescu, M., Licandro, J., Morate, D., et al. 2016, *A&A*, 591, A115
- Popova, O. P., Jenniskens, P., Emel'yanenko, V., et al. 2013, *Science*, 342, 1069
- Pravec, P., Hergenrother, C., Whiteley, R., et al. 2000, *Icarus*147, 477
- Pravec, P., Harris, A. W. 2000, *Icarus*148, 12
- Pravec, P., Harris, A. W., Scheirich, P., et al. 2005, *Icarus*, 173, 108
- Pravec, P., Scheirich, P., Ďurech, J., et al. 2014, *Icarus*, 233, 48
- Rozitis, B., MacLennan, E., & Emery, J. P. 2014, *Nature*, 512, 1174
- Sako, S., Ohsawa, R., Takahashi, H., et al. 2016, *Proc. SPIE*, 9908, 15
- Sako, S., Ohsawa, R., Takahashi, H., et al. 2018, *Proc. SPIE*, 10702, 17

- Samarasinha, N. H., & A'Hearn, M. F. 1991, *Icarus*, 93, 194
- Scargle, D. J. 1982, *ApJ*, 263, 835
- Scheeres, D. J., Marzari, F., & Rossi, A. 2004, *Icarus*, 170, 312
- Scheirich, P., Āurech, J., Pravec, P., et al. 2010, *Meteoritics & Planetary Science*, 45, 1804
- Sharma, I., Burns, J. A., & Hui, C.-Y. 2005, *MNRAS*, 359, 79
- Sonka, A. B., Gornea, A. J., Anghel, S., & Birlan, M. 2017, *Romanian Astronomical Journal*, 27, 223
- Takahashi, J., Urakawa, S., Terai, T., et al. 2014, *PASJ*, 66, 53
- Tan, H., & Gao, X. 2018, *The Minor Planet Bulletin*, 45, 220
- Tonry, J. L. 2011, *Publications of the Astronomical Society of the Pacific*, 123, 58
- Toricarico, P. 2017, *Icarus*, 284, 416
- Trilling, D. E., Valdes, F., Allen, L., et al. 2017, *AJ*, 154, 170
- Usui, F., Kasuga, T., Hasegawa, S., et al. 2013, *ApJ*, 762, 56
- Vereš, P., Jedicke, R., Fitzsimmons, A., et al. 2015, *Icarus*, 261, 34
- Wainscoat, R., Veres, P., Bolin, B., et al. 2014, in *Asteroids, Comets, Mereors –Book of Abstracts*, ed. K. Muinonen et al. (Finland: Helsinki), 574
- Warner, B. D., Harris, A. W., & Pravec, P. 2009, *Icarus*, 202, 134
- Warner, B. D. 2014, *The Minor Planet Bulletin*, 41, 113
- Warner, B. D. 2015, *The Minor Planet Bulletin*, 42, 115
- Warner, B. D. 2018, *The Minor Planet Bulletin*, 45, 19
- Warner, B. D., & Pravec, P. 2018, *The Minor Planet Bulletin*, 45, 259
- Zappalà, V., Cellino, A., Barucci, A. M., et al. 1990, *A&A*, 231, 548
- Zappalà, V., Cellino, A., Dell'Oro, A. 2002, *Icarus*, 157, 280